Rate-dependent strength and ductility of binder jetting 3D-printed stainless steel 316L: Experiments and modeling

Author(s):
Tancogne-Dejean, Thomas; Roth, Christian C.; Mohr, Dirk

Publication date:
2021-10-01

Permanent link:
https://doi.org/10.3929/ethz-b-000499565

Originally published in:
International Journal of Mechanical Sciences 207, https://doi.org/10.1016/j.ijmecsci.2021.106647

International Journal of Mechanical Sciences 207 (2021) 106647

Contents lists available at ScienceDirect

International Journal of Mechanical Sciences

journal homepage: www.elsevier.com/locate/ijmecsci

Rate-dependent strength and ductility of binder jetting 3D-printed stainless steel 316L: Experiments and modeling

Thomas Tancogne-Dejean, Christian C. Roth, Dirk Mohr*

Department of Mechanical and Process Engineering, ETH Zurich, Switzerland

ARTICLE INFO

Keywords:
Additive manufacturing
Stainless steel
Ductile failure
Strain rate sensitivity
Binder jet printing

ABSTRACT

Binder-jetting is an additive manufacturing process for metals which involves the rapid making of a binder bonded metal powder part followed by the removal of the binder and creation of a fully dense part in a subsequent sintering step. This emerging process has the potential of high cost efficiency as compared to selective laser melting (SLM) or shaped metal deposition. Here, we determine the rate-dependent plasticity and fracture properties of binder-jetted stainless steel 316L. Electron Back-Scattered Diffraction (EBSD) analysis and tomography revealed an equi-axed grain structure with an initial porosity of 3%. The latter is due to pores with an average size of 20μm that are clustered in layers perpendicular to the build direction. The observed stress-strain curve of the binder-jetted material always lies below that of wrought stainless steel 316L with a 50% lower initial yield stress and a 30% lower ultimate strength. Both the material anisotropy and strain rate sensitivity may be considered as second order effects in that comparison. The equivalent plastic strain obtained from fracture experiments for different stress states is also always lower for the binder-jetted material. The observations for the binder-jetted material therefore stand in stark contrast to those for SLM-made stainless steel which can provide an even higher yield strength than the wrought material. From a mechanism point of view, the low mechanical properties of the binder-jetted material may be explained by the high initial porosity which is reminiscent of cast metals.

1. Introduction

Over the last decade, Additive Manufacturing (AM) techniques have become a field of major interest both in research as well as in industrial applications. After its successful application for rapid prototyping, the technology has reached a level of maturity to serve as manufacturing technique. Previously unobtainable structures can now be manufactured with the help of AM [1], thereby finding their way into engineering applications [2,3]. Among the seven categories of additive manufacturing techniques defined in the ASTM F42 standard, direct energy deposition and powder bed fusion are the most widely-used for metals. In particular, 3D printing techniques such as direct metal laser sintering (DMLS) [4], electron beam melting (EBM) [5], selective heat sintering (SHS), selective laser sintering (SLS) [6] or selective laser melting (SLM) [7] are well-established. It is only recently that binder jetting receives increased attention, mostly because of its potential of reducing the costs of additively-manufactured metallic parts.

Instead of selectively-joining the particles of a metal powder through melting, a liquid polymer binding agent is delivered layer-by-layer to a powder bed to build the part [8]. The so-called “green part” composed of bonded metal particles is then obtained after curing the binding agent and removing the excess powder in a so-called “decaking” step. Subsequently, the metallic final part is then obtained through a sintering process during which the polymer binder evaporates and metal-metal joints are formed. Aside from reduced printer and powder cost, binder jetting is significantly faster than SLM. Furthermore, a wide range of materials is available since almost any metal injection molding powder can be used [9]. Higher throughput than for SLM is obtained through part stacking. Due to the binder, no support structures are needed which allows for a higher design freedom. The sintering process also produces more isotropic material properties and a more conventional grain structure than the inevitable rapid-quenching during SLM. The known disadvantages of the binder jetting technique are the high porosity of the final part and part shrinkage during sintering [10].

Stainless-steel 316L is one of the most widely studied materials for additive manufacturing. For example, Bronkhorst et al. [11] reported a 1.7 times higher flow stress for selective laser melted stainless steel 316L than its wrought counterpart. Li et al. [11] observed an over 60% higher yield stress and a higher strain rate sensitivity when comparing SLM and cold-rolled SS316L. A significant decrease in the yield strength of an SLM manufactured 316L was described by [12] when performing heat treatments on the material, which was also reported in [13]. Wilson-Heid et al. [14] investigated the large deformation behavior of SLM manufactured 316L for five stress states in [14]. Consistent with the

* Corresponding author.
E-mail address: mohr@mit.edu (D. Mohr).

https://doi.org/10.1016/j.ijmecsci.2021.106647
Received 9 April 2021; Received in revised form 22 June 2021; Accepted 4 July 2021
Available online 15 July 2021

findings of [12] and [15], they found that the Hosford-Coulomb fracture initiation model is able to accurately capture the stress-state dependent fracture response. Several authors have investigated SLM 316L over a range of strain rates [11,15] finding moderate strain rate sensitivity between 0.012- 0.025 for strain rates up to 1000/s.

Kumar et al. ([16]) investigated the tensile response and high-cycle fatigue of binder jetted 316L and compared it to SLM and conventionally manufactured (hot-rolled and air-cooled) counterparts. They found a high degree of similarity between the binder jetted and the hot rolled material, especially with respect to the hardening and fatigue response, which is explained by the similarities in the planar slip deformation mechanism and the absence of severe local thermal gradients during the manufacturing process. Another noteworthy aspect is the transformation of austenite to martensite induced by plastic deformation [17]. It was shown by Paredes et al. [18] that this effect becomes most prominent at cryogenic temperatures.

In the present study, the strain rate and stress-state dependent plasticity and fracture properties of binder jetting manufactured stainless steel 316L are investigated. The experimental campaign on three different material batches covers stress states from shear to equi-biaxial tension. It comprises low, intermediate and high strain rate experiments covering strain rates ranging from 0.001/s to several 100/s. Micro-computed tomography as well as electron microscope fractography and Electron Back-Scattered Diffraction (EBSD) are performed. A modified Johnson-Cook type plasticity model with a Hill'48 non-associated flow rule and a Hosford-Coulomb fracture initiation model are identified based on the experimental results.

2. Material and experiments

2.1. Binder jetting manufacturing

All binder jetting parts are made from a stainless steel 316L powder by our industrial partners. The powder deposition process is set up with a layer thickness of 70μm. The sintering is performed in a hydrogen-filled batch oven at 1380°C. Three batches of 60mm x 200mm large plates are manufactured, denoted as batch #1, #2 and #3. The first two batches feature a plate thickness of 1.2mm, while the third batch exhibits a thickness of 1.0*mm*. Furthermore, to assess the mechanical properties of bulk components, a batch of blocks with the dimensions of 65mm x 65mm x 10mm is manufactured.

2.2. Material characterization

2.2.1. Micro-computed tomography

Micro-Computed Tomography (micro-CT) is performed to evaluate the porosity content and spatial distribution of voids in the material. The micro-CT scan is performed in an XT H 225 ST (Nikon) lab tomograph. The voxel size is 2.8μm and pores are reconstructed with a minimum volume of eight voxels. The volume and the center position of each pore is extracted and an average pore radius is computed based on the volume-equivalent sphere. To attain the maximum achievable resolution, a 1.8*mm*-diameter cylinder of 1*mm* height specimen is extracted using wire-EDM.

2.2.2. Scanning electron microscopy

A Scios SEM (FEI) operating at 20kV with a beam current of 13nA is used to obtain crystallographic information of the undeformed material using Electron Backscattered Diffraction (EBSD) in the in-plane and out-of-plane directions. The samples for EBSD are prepared by grinding with silicon carbide paper, followed by polishing with diamond suspension down to a particle diameter of 3μm and finally polishing with alumina colloid with a particle size of 60nm. The electron beam spot size is set to 1.0μm. The same operating parameters are used to investigate the fracture surface of selected mechanical tests.

2.3. Mechanical experiments

2.3.1. Specimen geometries

Different types of specimens (Fig. 1) are extracted from the additively-manufactured parts to characterize the plasticity and fracture properties of the material:

(i) Uniaxial tension specimens (UT) featuring a 20mm long and 10mm wide gauge section.
(ii) Notched tensile specimens with a cutout radius of 6*mm* (NT6), an outer gauge section width of 20mm and a central gauge section width reduced to 10mm due to the two round cutouts.
(iii) Single gauge section shear tests (SH) following the "medium ductility" geometry of [19]
(iv) Mini-punch (MP) and mini-Nakazima (MN) with the geometries described in [20] and [21].

The UT specimens are extracted along the long direction (UT0), at an angle of 45 degrees (UT45) and 90 degrees (UT90) for batches #1, #2 and #3. To assess any gradient in mechanical properties through the thickness, the thick plates are sliced into 1mm-thick sheets using wire Electric Discharge Machining (wire-EDM) before extracting UT0 specimens. The NT6 and SH specimens are extracted from the thin plates with the loading direction aligned with the long direction of the plate. Due to the limited material availability, all other tests are only performed for batch #1. This includes the MP and MN specimens as well as UT, NT6 and SH specimens for intermediate and fast loading (Fig. 1a–c).

2.3.2. Experimental procedures

2.3.2.1. Slow and intermediate strain rate experiments. All experiments at slow and intermediate strain rates are performed on a hydraulic universal testing machine (Instron 8801) equipped with a 100*kN* load cell. For the tensile testing (UT, NT6, SH), custom-made high-pressure clamps are used. A constant crosshead speed of 2.4mm/min (slow) and 2400mm/min (intermediate) is used for the UT specimens resulting in strain rate of 0.002/s and 2/s, respectively. A lower speed of 0.4mm/min and 400 mm/min is used to attain similar equivalent plastic strain rates in the NT6 and SH experiments.

In all experiments, the deformation field is monitored using Digital Image Correlation (VIC2D, Correlated Solutions) after applying a black and white speckle pattern onto the specimen surface. For the slow experiments, a 5Mpx camera (Point Grey GS3-U3-51S5M-C equipped with 100mm 1:1 Tokina macro lenses) is used to record the deformation at a frequency of 1Hz. The pixel size is 19μm, 33 μm and 8 μm for the UT, NT6 and SH respectively. For the intermediate speed experiments, a high speed camera (Photron SA-Z) is used with a resolution of 1024 × 1024 pixels at 2000Hz, resulting in a spatial resolution of 48.2μm/pixel (UT and NT6) and 19.9μm/pixel (SH). In addition to the optical measurements through DIC, a high-speed infrared camera (FLIR X6801SC) operating at a rate of 1995fps is used to measure the evolving temperature field on the specimen surface with a 50mm F/3 Bayonet (T199082) and a spatial resolution of 131μm/pixel.

The out-of-plane tests (MP, MN) are performed using a custom-made loading device [20,21] with a crosshead speed of 2mm/min. The local deformation of the specimens is monitored using 3D-DIC (VIC3D, Correlated Solutions) with an optical system composed of twice the camera and lens used for the tensile testing. The acquisition frequency is set to 1Hz.

2.3.2.2. High strain rate experiments. The high strain rate experiments are performed on a split Hopkinson pressure bar system (SHPB) equipped with a load inversion device [22]. The testing system includes a striker bar (4990mm long, 20mm diameter), an input bar (5927mm long, 20mm diameter), a load-inversion device and an output bar (5951mm long, 20mm diameter) made from steel. Fig. 2 depicts the experimental set-up. It includes a load inversion device composed of a stirrup and a pusher. The specimen is bolted onto the pusher on the

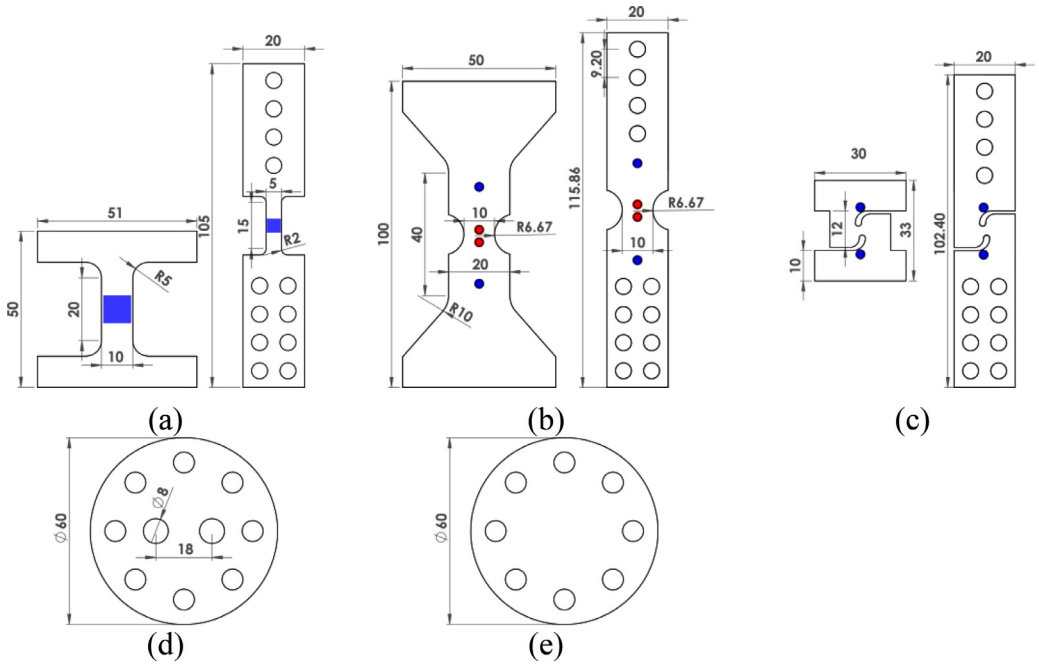

Fig. 1. Sketch of the specimens for plasticity and fracture characterization. (a) Uniaxial Tension (UT), (b) Notched tension (NT6), (c) shear (SH), (d) Mini-Nakazima (MN), (e) Mini-Punch (MP) For UT, NT6 and SH the samples are for slow/intermediate and high strain rates from left to right.

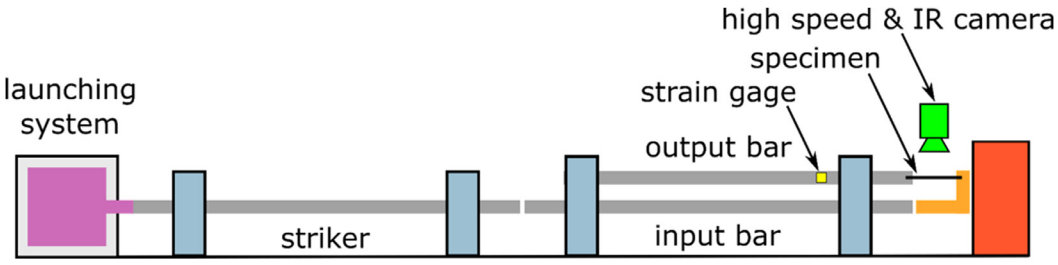

Fig. 2. Schematic of the Split Hopkinson Pressure Bar with the load inversion device (orange) and the data acquisition equipment. (For interpretation of the references to color in this figure legend, the reader is referred to the web version of this article.).

incident shoulder by a set of eight M5 screws, while it is directly fixed onto the output bar using four M5 screws. Strain gauges are glued onto the output bar at a distance of 430mm from the specimen/output bar interface to measure the axial force histories $F_{out}[t]$. The force history is estimated using

$$F_{out}[t] = E_{out} A_{out} \varepsilon_{tra}[t] \tag{1}$$

with a Young's modulus E_{out} = 204.7GPa and the cross-section areaA_{out} = 312.8mm^2 of the output bar. In the high strain rate experiments, the Photron SA-Z is operated at a resolution of 512 × 260 pixels to allow for an imaging frequency of 120kHz with a spatial resolution of 71µm/pixel. The high-speed IR camera (FLIR X6801SC) is employed with an acquisition frequency of 7079Hz to observe the temperature evolution along a line at the center of the specimen. The corresponding spatial resolution for the infrared imaging is 88.3µm/pixel. All data and image acquisitions are triggered by a rise in the input force signal above a threshold value to synchronize the electronic and optical measurements.

Virtual extensometers with a length of 30mm (NT6) and 13mm (SH) are used to report the displacement of the specimen shoulders. Furthermore, a 2mm-long extensometer is positioned at the center of the NT6 gauge section to record the history of the local axial strain. Furthermore, the axial and transverse strains are evaluated in a 9mm x 9mm (4.8mm x 4.8mm at high strain rates) area at the center of the gage section of the UT specimens. Based on these measurements, the Lankford ratios are determined (Fig. 7c). The use of an area extensometer yields average properties, thereby compensating for local strain field fluctuations related to possible material heterogeneities. The Lankford ratio is defined through the ratio of the incremental width to thickness plastic strain

$$r = \frac{d\varepsilon_w^p}{d\varepsilon_t^p} = -\frac{d\varepsilon_w^p}{d\varepsilon_a^p + d\varepsilon_w^p} \tag{2}$$

where ε_a^p, ε_w^p and ε_t^p are the plastic strain in the axial, width and through thickness directions. The latter is computed assuming plastic incompressibility, while the Lankford ratio is obtained through linear regression of the width vs thickness strain plot. The yield stress of the material is defined as the stress at 0.2% of plastic deformation.

3. Computational modeling

The material is modeled as an anisotropic elasto-plastic material with self-similar (isotropic) hardening. The material elasticity is assumed to be isotropic and is described by the Young's modulus E and Poisson's ratio ν. The possible effects of phase transformation and kinematic hardening are neglected.

3.1. Yield function and flow rule

The von Mises yield function is used along with a non-associated Hill'48 flow rule. Introducing the deformation resistance k, the yield

function reads

$$f[\boldsymbol{\sigma}, k] = \bar{\sigma}_{vM} - k = 0 \tag{3}$$

with von Mises equivalent stress $\bar{\sigma}_{vM} = \bar{\sigma}_{vM}[\boldsymbol{\sigma}]$ and the Cauchy stress vector

$$\boldsymbol{\sigma} = \begin{bmatrix} \sigma_{11} & \sigma_{22} & \sigma_{33} & \sigma_{12} & \sigma_{23} & \sigma_{13} \end{bmatrix}^T. \tag{4}$$

We denote the plastic strain vector $\boldsymbol{\epsilon}^p$as

$$\boldsymbol{\varepsilon}^p = \begin{bmatrix} \varepsilon^p_{11} & \varepsilon^p_{22} & \varepsilon^p_{33} & 2\varepsilon^p_{12} & 2\varepsilon^p_{23} & 2\varepsilon^p_{13} \end{bmatrix}^T. \tag{5}$$

The flow rule is defined as

$$\dot{\boldsymbol{\varepsilon}}^p = \dot{\lambda}\frac{dg}{d\boldsymbol{\sigma}} \tag{6}$$

where $\dot{\lambda}$ is the plastic multiplier and $g = \sqrt{(\mathbf{G}.\boldsymbol{\sigma})\boldsymbol{\sigma}}$ with

$$\mathbf{G} = \begin{pmatrix} 1 & G_{12} & -(1+G_{12}) & 0 & 0 & 0 \\ G_{12} & G_{22} & -(G_{12}+G_{22}) & 0 & 0 & 0 \\ -(1+G_{12}) & -(G_{12}+G_{22}) & 1+2G_{12}+G_{22} & 0 & 0 & 0 \\ 0 & 0 & 0 & G_{33} & 0 & 0 \\ 0 & 0 & 0 & 0 & 3 & 0 \\ 0 & 0 & 0 & 0 & 0 & 3 \end{pmatrix} \tag{7}$$

The equivalent plastic strain rate is defined as the work-conjugate to the equivalent stress

$$\dot{\bar{\varepsilon}}_p = \frac{\boldsymbol{\sigma} : \dot{\boldsymbol{\varepsilon}}^p}{\bar{\sigma}_{Hill'48}}. \tag{8}$$

The non-associated flow rule is fully determined by the choice of the three material parameters $\{G_{12}, G_{22}, G_{33}\}$. The model is reduced to an isotropic Levy-von Mises plasticity for $G_{12} = -0.5$, $G_{22} = 1.0$ and $G_{33} = 3.0$.

3.2. Incorporation of strain rate and temperature effects

The deformation resistance in Eq. (3) is defined as a multiplicative composition of a strain hardening, a strain rate hardening and a temperature softening term,

$$k\left[\bar{\varepsilon}_p, \dot{\bar{\varepsilon}}_p, T\right] = k_{SV}\left[\bar{\varepsilon}_p\right] k_{\dot{\bar{\varepsilon}}_p}\left[\dot{\bar{\varepsilon}}_p\right] k_T[T]. \tag{9}$$

The isotropic strain hardening is described by a linear combination of a power law (Swift, 1952 [23]) and exponential (Voce, 1948 [24]) hardening given by the following equation ([25,26]):

$$k_{SV}(\bar{\varepsilon}^p) = \alpha A\left(\varepsilon_0 + \bar{\varepsilon}^p\right)^n + (1-\alpha)\left(k_0 + Q(1 - \exp(-\beta\bar{\varepsilon}^p))\right) \tag{10}$$

This parametric hardening law features three parameters for the Swift term $\{A, \varepsilon_0, n\}$, three parameters for the Voce term $\{k_0, Q, \beta\}$ and a weighting parameter bound to $\alpha \in [0, 1]$.

Following Johnson and Cook [27], the strain rate hardening term $k_{\dot{\bar{\varepsilon}}_p}[\dot{\bar{\varepsilon}}_p]$ is written as

$$k_{\dot{\bar{\varepsilon}}_p}\left[\dot{\bar{\varepsilon}}_p\right] = \begin{cases} 1 & for \quad \dot{\bar{\varepsilon}}_p < \dot{\varepsilon}_0 \\ 1 + C\ln\left[\frac{\dot{\bar{\varepsilon}}_p}{\dot{\varepsilon}_0}\right] & for \quad \dot{\bar{\varepsilon}}_p \geq \dot{\varepsilon}_0 \end{cases} \tag{11}$$

with C the strain rate sensitivity parameter and $\dot{\varepsilon}_0$ the reference strain rate. The thermal softening term $k_T[T]$ is described as

$$k_T[T] = \begin{cases} 1 & for \quad T < T \\ 1 - \left(\frac{T - T_r}{T_m - T_r}\right)^m & for \quad T_r \leq T \leq T_m \end{cases}. \tag{12}$$

Herein m is the thermal softening coefficient, T_r the room temperature and T_m the melting temperature of the material.

The temperature is treated as an internal state variable (as suggested in [28]), with its evolution estimated using the function

$$dT = \omega\left[\dot{\bar{\varepsilon}}_p\right]\frac{\eta_k}{\rho C_p}\bar{\sigma}_{Hill}d\bar{\varepsilon}_p. \tag{13}$$

It comprises η_k, the Taylor-Quinney coefficient, ρ, the mass density and C_p the specific heat capacity of the material. To incorporate the transition from isothermal to adiabatic conditions, the strain rate dependent function $\omega[\dot{\bar{\varepsilon}}_p]$ is introduced

$$\omega\left[\dot{\bar{\varepsilon}}_p\right] = \begin{cases} 0 & for \quad \dot{\bar{\varepsilon}}_p < \dot{\varepsilon}_{it} \\ \frac{\left(\dot{\bar{\varepsilon}}_p - \dot{\varepsilon}_{it}\right)^2\left(3\dot{\varepsilon}_a - 2\dot{\bar{\varepsilon}}_p - \dot{\varepsilon}_{it}\right)}{\left(\dot{\varepsilon}_a - \dot{\varepsilon}_{it}\right)^3} & for \quad \dot{\varepsilon}_{it} \leq \dot{\bar{\varepsilon}}_p \leq \dot{\varepsilon}_a \\ 1 & for \quad \dot{\varepsilon}_a < \dot{\bar{\varepsilon}}_p \end{cases}, \tag{14}$$

with $\dot{\varepsilon}_{it}$ and $\dot{\varepsilon}_a$ describing the isothermal and adiabatic limit strain rates, respectively. For ease of calibration, the isothermal limit strain rate is chosen to be the same as the reference strain rate $\dot{\varepsilon}_0$ from the strain rate hardening term.

3.3. Ductile fracture modeling

Two measures are introduced to measure the stress state. Firstly, the stress triaxiality η is defined by the ratio of the mean stress σ_m and the von Mises equivalent stress $\bar{\sigma}_{vM}$,

$$\eta = \frac{\sigma_m}{\bar{\sigma}_{vM}}. \tag{15}$$

Secondly, the Lode angle parameter is introduced to characterize the effect of the third deviatoric stress tensor invariant J_3,

$$\bar{\theta} = 1 - \frac{2}{\pi}\arccos\left[\frac{27}{2}\frac{J_3}{\bar{\sigma}^3_{vM}}\right]. \tag{16}$$

According to the Hosford-Coulomb model [29], ductile fracture is expected to initiate when the equivalent plastic strain satisfies the following integral condition

$$\int_0^{\bar{\varepsilon}^p_f} \frac{d\bar{\varepsilon}^p}{\bar{\varepsilon}^{pr}_f(\eta, \bar{\theta})} = 1 \tag{17}$$

where

$$\bar{\varepsilon}^{pr}_f[\eta, \bar{\theta}] = b(1+c)^{\frac{1}{n}} \times \left(\left\{\frac{1}{2}\left((f_1 - f_2)^a + (f_2 - f_3)^a + (f_1 - f_3)^a\right)\right\}^{\frac{1}{a}} + c(2\eta + f_1 + f_3)\right)^{-\frac{1}{n}} \tag{18}$$

With the Lode angle parameter dependent trigonometric functions

$$f_1\left[\bar{\theta}\right] = \frac{2}{3}\cos\left[\frac{\pi}{6}(1 - \bar{\theta})\right],\ f_2\left[\bar{\theta}\right] = \frac{2}{3}\cos\left[\frac{\pi}{6}(3 + \bar{\theta})\right] \text{ and } f_3\left[\bar{\theta}\right] = -\frac{2}{3}\cos\left[\frac{\pi}{6}(1 + \bar{\theta})\right] \tag{19}$$

The fracture model is characterized by three main parameters $\{a, b, c\}$. The Hosford exponent a controls the effect of the Lode angle, while the friction coefficient c accounts for the effect of the stress triaxiality on failure. The parameter b is a scaling factor that is defined such that it corresponds to the failure strain for proportional uniaxial (or equibiaxial) tensile loading. The parameter n has only a little influence on the fracture locus as any change of its value can be compensated by a change in $\{a, b\}$. It is therefore fixed to $n = 0.1$ ([29]).

3.4. Finite element models

Finite element simulations are performed for identifying and validating the plasticity and fracture models. The simulations are carried out using the finite element software Abaqus/explicit for the NT6 and SH specimens. Exploiting the symmetries of the specimen, only one-eighth of the model is meshed with first-order reduced integration elements (C3D8R from Abaqus library) for the NT6 and only half for the SH specimen. The specimen models feature eight elements along the thickness direction and an edge length of 0.1mm in the plane of the specimen. The

meshes are shown in Fig. 15. Mass scaling is used to reduce the computational time, while ensuring that the kinetic energy is small compared to the internal energy. The force as well as the global and local displacements are extracted for the same extensometer positions as in the experiments. The stress state and equivalent plastic strain of the most critical elements are extracted for fracture characterization.

3.5. Material model identification

According to the above models, the elastic, plastic and fracture properties of the material are determined through 18 material constants. The elastic constants are provided by the manufacturer. All other model parameters are identified from the experiments on the thin plates from batch #1.

3.5.1. Plasticity model identification

The flow rule parameters are calibrated based on the uniaxial tensile experiments. Using Eq. (6), the Lankford ratios are related to the flow rule using the following equation

$$r(\varphi) = \frac{\left(G_{33} + 2G_{12} - G_{22} - 1\right)\sin^2(\varphi)\cos^2(\theta) - G_{12}}{\left(1 - G_{22}\right)\cos^2(\varphi) + G_{12} + G_{22}}. \tag{20}$$

where φ is the angle between the build direction and the loading axis of the specimen.

For the tests performed at 0°, 45° and 90°, Eq. (20) can be reduced and inverted to obtain the following values of the flow rule parameters:

$$\begin{aligned} G_{12} &= -\frac{r(0)}{1+r(0)}, \\ G_{22} &= \frac{r(0)}{r(90)}\frac{1+r(90)}{1+r(0)}, \\ G_{33} &= \frac{1+2r(45)}{r(90)}\frac{r(0)+r(90)}{1+r(0)} \end{aligned} \tag{21}$$

Given the isotropic yield stress, both Swift and Voce hardening laws are calibrated on a test representative of the average of all UT true stress-true strain curve through a least-square error minimization. Finally, the weighting parameter α as well as the strain rate and temperature parameters (C, m, T_m, $\dot{\varepsilon}_a$) are computed using an inverse calibration procedure. The inverse calibration consists of coupled Abaqus simulations of the NT6 experiments at all speeds with a gradient-free Nelder-Mead algorithm implemented in Matlab to minimize the root mean square error between the NT6 experimental and simulated force displacement response. Standard values are chosen for the remaining constants [11].

3.5.2. Fracture model parameter identification

The loading paths to fracture $\{\eta, \bar{\theta}, \bar{\varepsilon}^p\}$ for the NT6 and SH are extracted from the numerical simulations at the element featuring the highest equivalent plastic strain. Furthermore, the equivalent plastic strain at fracture for the MP and MN are obtained from the full field 3D-DIC, where the stress state is proportional throughout the experiments. The calibration is performed using a least-square fit of the Hosford-Coulomb fracture initiation model along the full loading paths. These loading cases allow to uniquely determine the three fracture parameters $\{a, b, c\}$.

4. Results

4.1. Microstructural analysis

Representative micro-CT images are shown in Fig. 3 for a sample whose cylinder axis was aligned with the build direction. The CT-image of a vertical plane (Fig. 3b) reveals that the pores are clustered within planes parallel to the building layers. This is tentatively attributed to binder diffusion issues. Within the build planes, the pores are randomly distributed and exhibit complex geometries (Fig. 3c). When moving to an adjacent plane (by 25μm along the cylinder axis, Fig. 3d), the porosity amount decreases significantly. Quantitative analysis with a bin size of 10μm (Fig. 4a) reveals that the porosity peaks about every 50μm when moving along the cylinder axis. Fig. 4b presents the volume of all pores within the CT-sample as a function of the average pore radius. The overall porosity content is about 3% of the total sample volume with most of the pores exhibiting a radius between 10μm and 20μm. It is re-

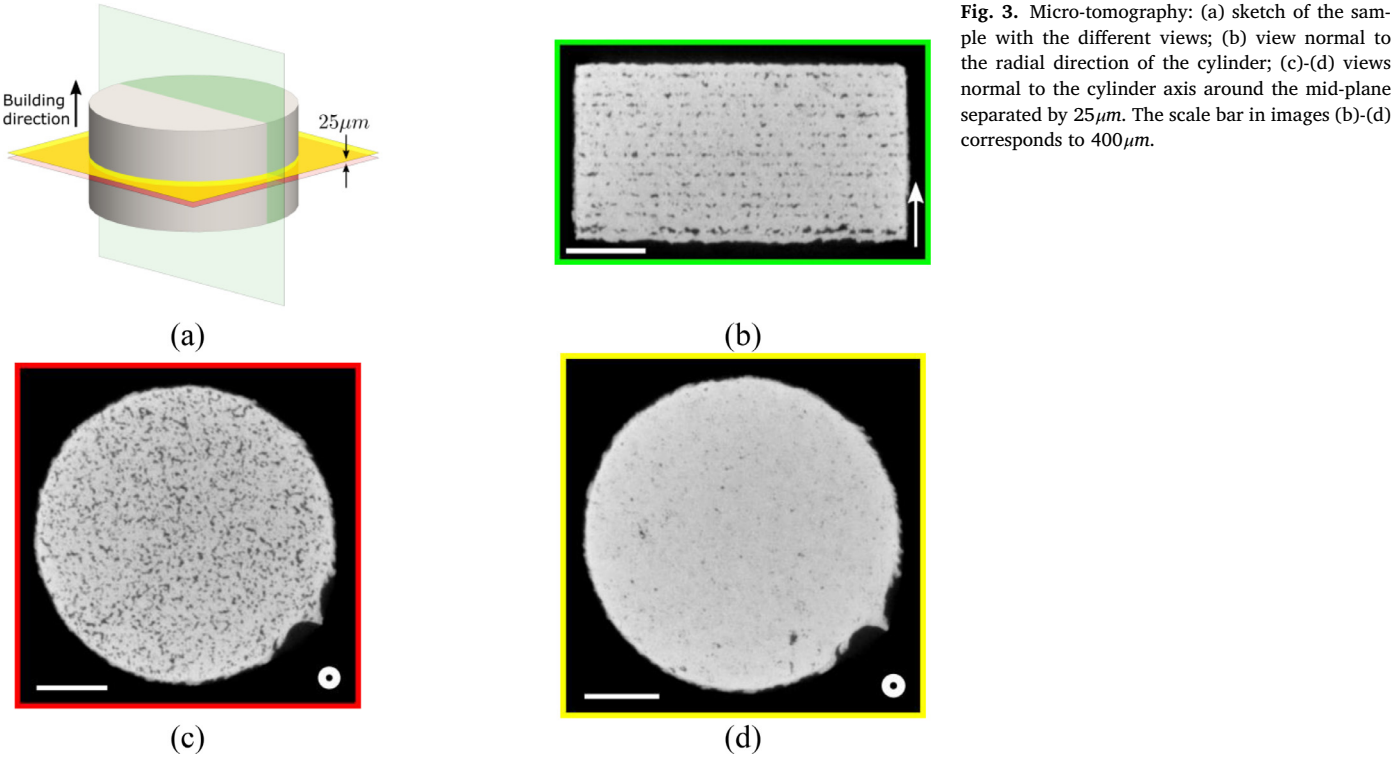

Fig. 3. Micro-tomography: (a) sketch of the sample with the different views; (b) view normal to the radial direction of the cylinder; (c)-(d) views normal to the cylinder axis around the mid-plane separated by 25μm. The scale bar in images (b)-(d) corresponds to 400μm.

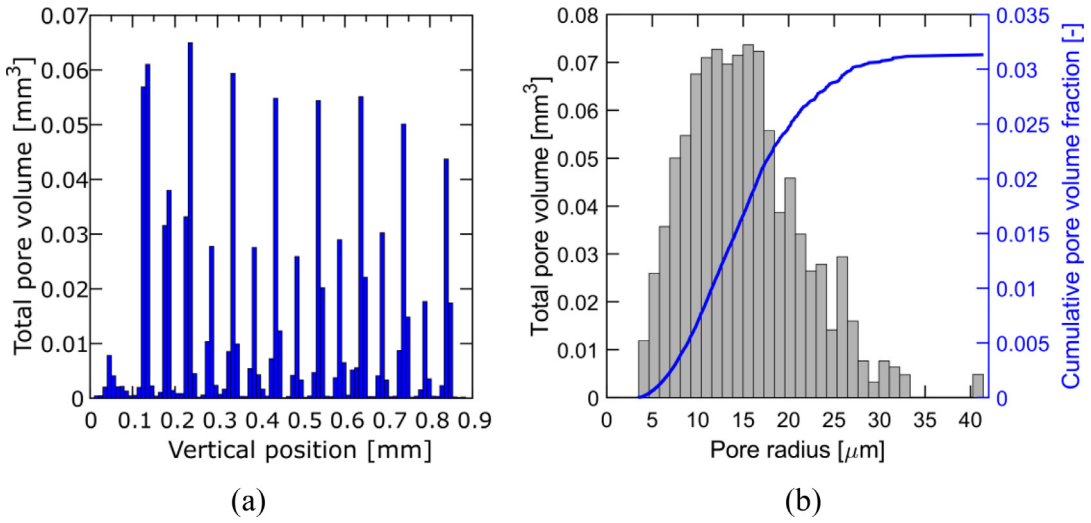

Fig. 4. Distribution of the pore volume fraction as a function of (a) the vertical position through the cylinder showing a layer spacing of approximately 50μm and (b) the average pore radius. The total pore volume fraction is around 3%.

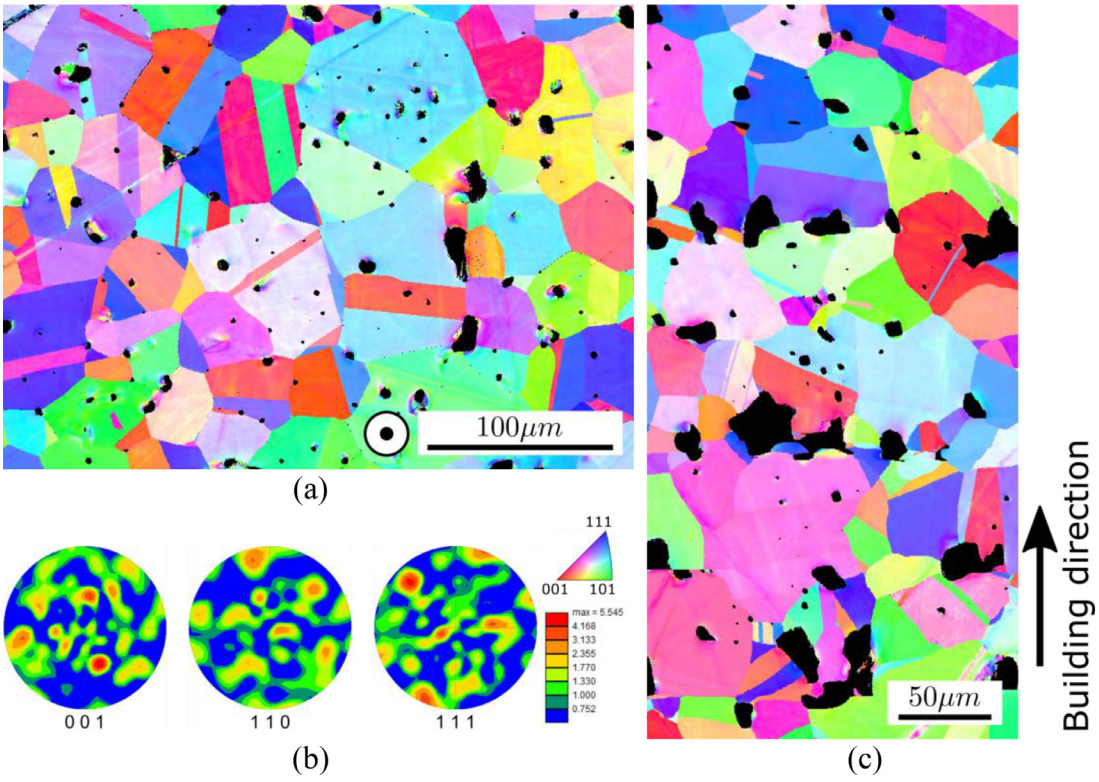

Fig. 5. Electron Backscattered Diffraction images of the binder-jetted material. (a) Inverse Pole Figure map (IPF) showing the grain size, crystallographic orientation and the presence of twins. (b) Pole figures of the same area. (c) IPF map in the out-of-plane direction highlighting the similar equi-axed grains and the porosity layers.

called that pores with a radius smaller than 3.5μm cannot be analyzed with the present CT-scan.

Selected EBSD analysis results are presented in Fig. 5. The inverse pole figures (Fig. 5a and c) reveal that the grains are approximately equi-axed with an average diameter of 50μm. Many annealing twins are visible. Both in-plane as well as out-of-plane large porosities are visible, the latter comprising three material layers separated by voids. The pole figures (Fig. 5b) show a weakly textured material. This is in agreement with the sintered nature of the material. The microstructure is vastly different from the one of SLM 316L stainless steel (e.g. [13]) in terms of crystal shape and texture and exhibits a lower texture than conventionally rolled 316L (e.g. [30]). Based on the micro-CT as well as the EBSD analysis, the binder jetting material is expected to exhibit a transversely isotropic mechanical response. Comparable EBSD results are obtained for all batches.

4.2. Results from macroscopic experiments

4.2.1. Uniaxial tension experiments

Fig. 6 presents the stress-strain curves from the UT tests for different directions of loading, batches and rates of loading. For batches #1/2 three repeats per direction are performed, while six are carried out for

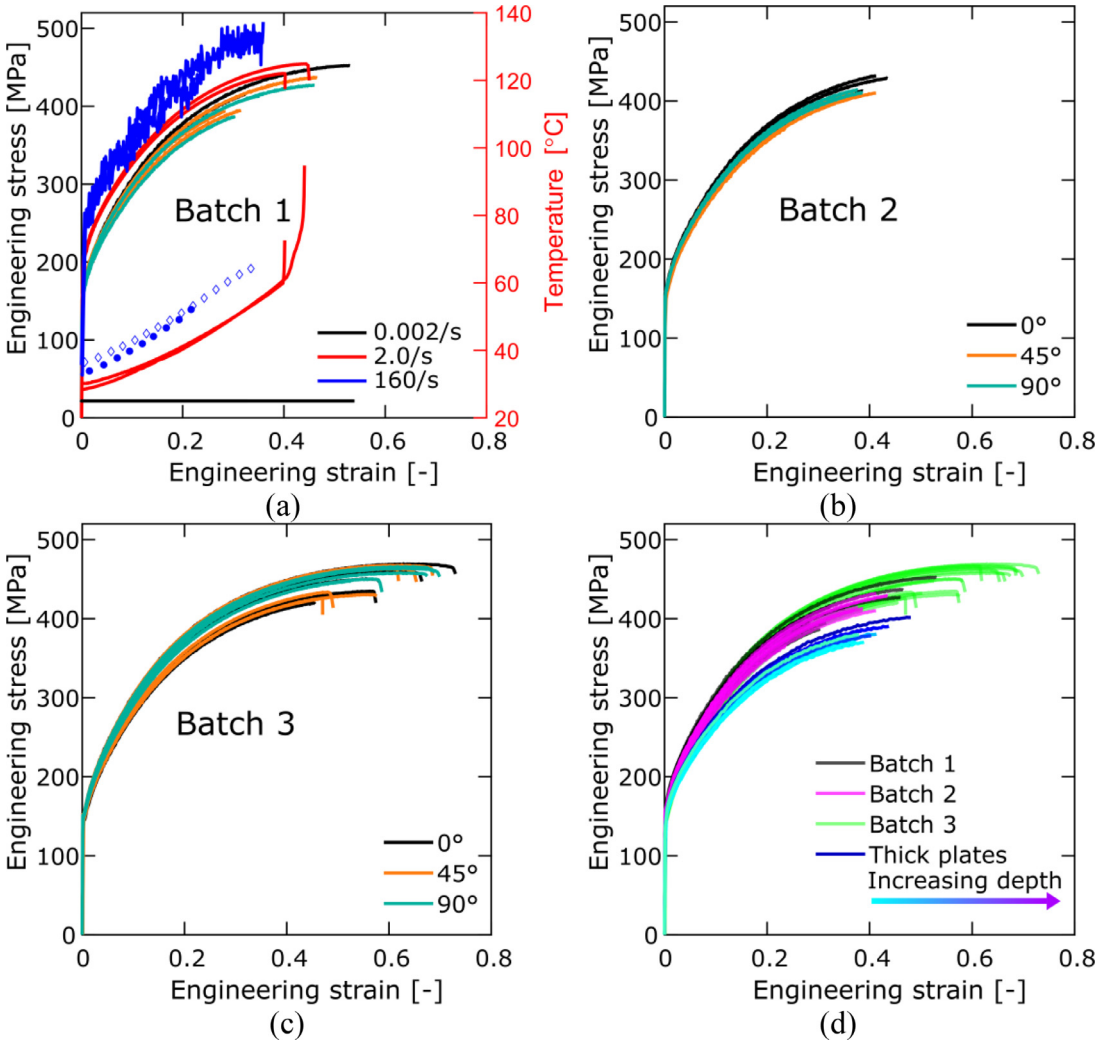

Fig. 6. Uniaxial tensile test results. (a) Batch 1 with direction and strain rate dependencies. Direction dependent stress strain curve for the second (b) and third (c) batch. (d) Summary of all tests along with the results from the samples extracted from the thick plates.

batch #3. Due to premature failure in the specimen shoulder, overall three samples are excluded from the analysis. The yield stress, ultimate tensile stress (UTS), true strain at maximum stress and Lankford ratios are reported in Fig. 7 through box and whisker plots for each batch. The material exhibits a low yield stress, around 150MPa for all batches, and a high hardening with a UTS (in true stress) between 567MPa and 700 MPa (batches #1/2 and batch #3). It should be noted that fracture occurs at maximum stress as seen in Fig. 6 and no necking is observed.

Overall, the specimens exhibit high ductility with a true strain at failure of 0.32 for the first two batches and 0.47 for batch #3, resulting in an average engineering strain at failure of 0.38 and 0.60, respectively. Fig. 6a–c depict the direction-dependent behavior of the UT specimens. No clear trends are visible in Fig. 6, which is confirmed by the box and whisker plots in Fig. 7, for the yield stress, UTS and true strain at failure. The Lankford ratios show a slight direction dependence with different behaviors for batches #1/2 and batch #3. For the first two batches, the average Lankford ratio decreases from 0° to 90° (from 0.84 to 0.79 for batch #1) while it slightly increases for batch #3 (from 0.85 to 0.87). However, it should be noted that the direction-dependence is rather weak, which indicates an anisotropic behavior mostly related to transverse anisotropy. Overall, the first two batches exhibit very similar mechanical properties, while the last batch differs by being slightly softer (8% lower yield stress) and more ductile (50% higher true strain at maximum stress); it also exhibits a slightly different direction dependence of the Lankford ratios.

The hardening behavior of all tests is shown in Fig. 8. A Swift law is fitted to all experiments and the extremal fits for each batch are used to create bands showing the spread of the data. It is noteworthy that the band for batch 2 falls well inside the band for batch 1, again underlining the repeatability of those two batches. Batch 3 exhibits a 3% higher hardening rate at a plastic strain of 0.8 compared to the first two batches.

Fig. 6d presents the results of the thick plate tests with increasing depth. No significant changes in mechanical properties are visible, which indicate that the sintering process did not lead to a through thickness gradient in the mechanical properties. The specimens extracted from the thick plates show an average yield stress of 154MPa, which is lower than the other batches, while the true strain at maximum stress reaches 0.33, which is on par with the first two batches. However, the specimens exhibit a lower hardening rate and thus a 5% lower ultimate tensile stress (average of 537MPa) compared to batches #1 and #2. No strong effect of the building height is visible and this difference is attributed to different build batches (e.g. compare batch #1/2 and #3).

Fig. 6a shows the results of the intermediate and high speed UT experiments. With the increase in strain rate, the overall stress level increases, with a stress (at 4% strain) of 238MPa at 0.002/s, 265 MPa at 2/s and 304MPa at 160/s, corresponding to about 13MPa increase per

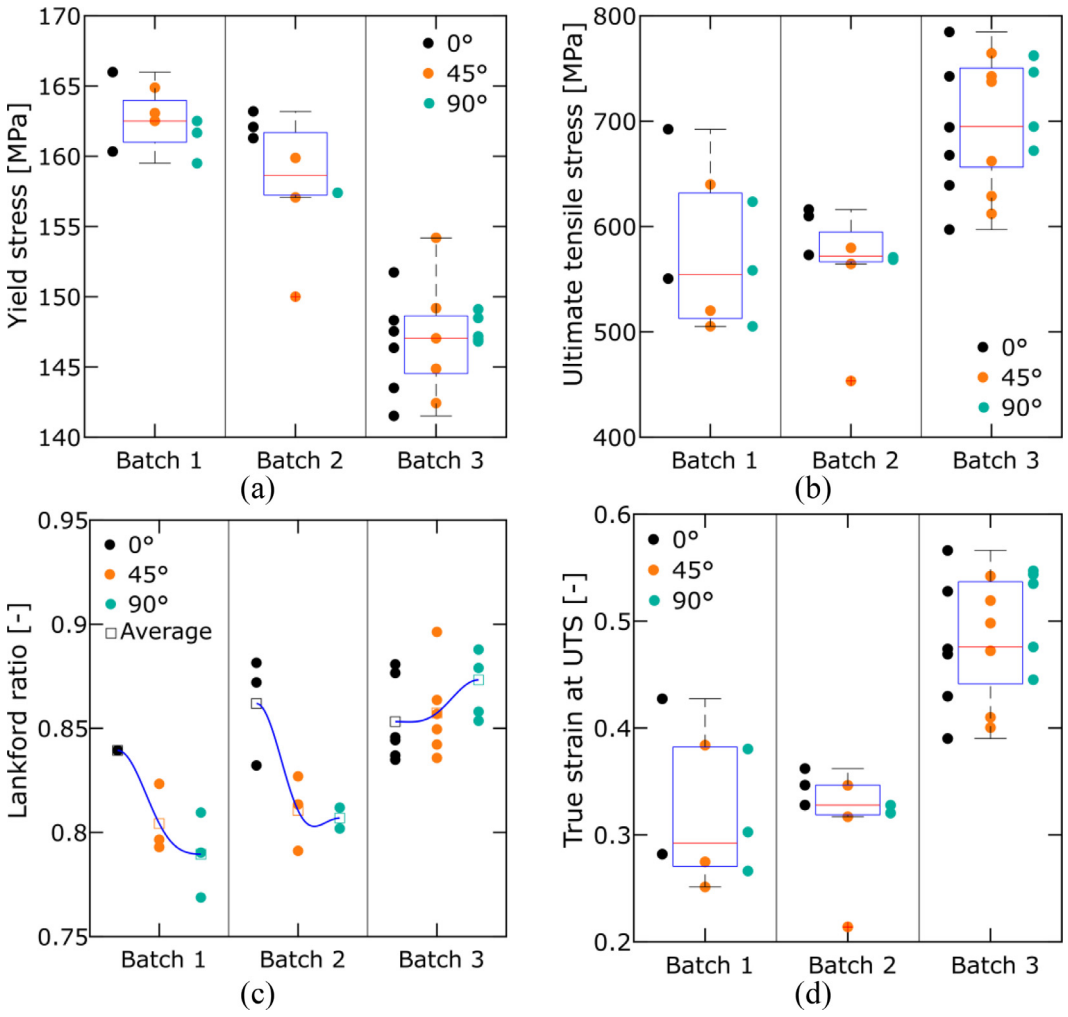

Fig. 7. Box-and-whisker plots representing the UT response of the different batches. (a) Yield stress, (b) Ultimate tensile stress (c) Lankford ratio and (d) true strain at UTS. The median is shown as a red line, while the blue box denotes the first and third quartile of the data. The black whiskers show the extremum values besides outliers, i.e. data points away by more than 1.5 times from the interquartile range. Note that the whisker plots consider all three orientation for each batch. (For interpretation of the references to color in this figure legend, the reader is referred to the web version of this article.).

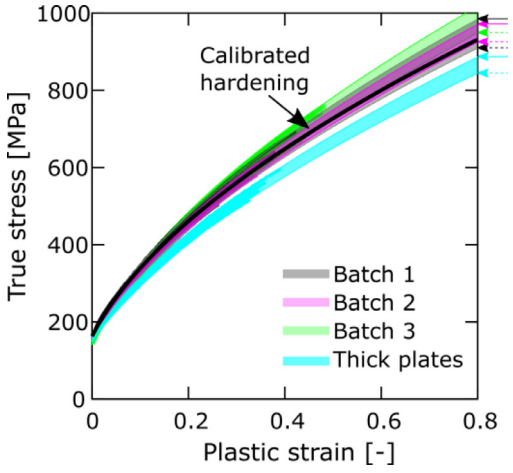

Fig. 8. Hardening response of all 3 batches and the thick plates. Each band corresponds to the lower and upper fit of the Swift laws for a given batch. The arrows on the right side denote the end of the respective band. The black line is the calibrated hardening curve for the finite element simulations.

decade. The hardening rate is similar for all speeds. The evolution of the maximum temperature on the specimen surface is reported on the secondary axis in Fig. 6a. For the intermediate and high speed experiments, an increase in temperature is observed with the increase in stress and strain. A good repeatability of the temperature evolution is observed at intermediate loading speed while more scatter is visible on the fast loading speed, which might be due to the limited field of view. The last instant before fracture is associated with a large increase in temperature, which cannot be captured for the high speed tests due to the relatively low frame rate of the IR camera. Temperatures between 60°C and 70°C are measured at the surface of the specimen before failure.

Full strain fields (obtained by DIC) are reported in Fig. 9 for representative UT samples loaded at different strain rates. The effective strain reported is defined as $\varepsilon_{eff} = \frac{2}{\sqrt{3}}\sqrt{\varepsilon_I^2 + \varepsilon_{II}^2 + \varepsilon_I \varepsilon_{II}}$ with ε_I and ε_{II} denoting the principal Hencky strains. The images are taken at different levels of strain, corresponding to an engineering strain of 0.05, 0.2 and the last image before failure. Fig. 9d shows the temperature field for the intermediate strain rate test. The deformation field is homogeneous for the slow strain rate test at all stages with a higher localization region in the middle of the specimen. However, for the intermediate and fast tests, even early into the experiment, the deformation is already localized in some specific regions of the sample and moves across the sample width during the course of the test. The temperature field correlates well with

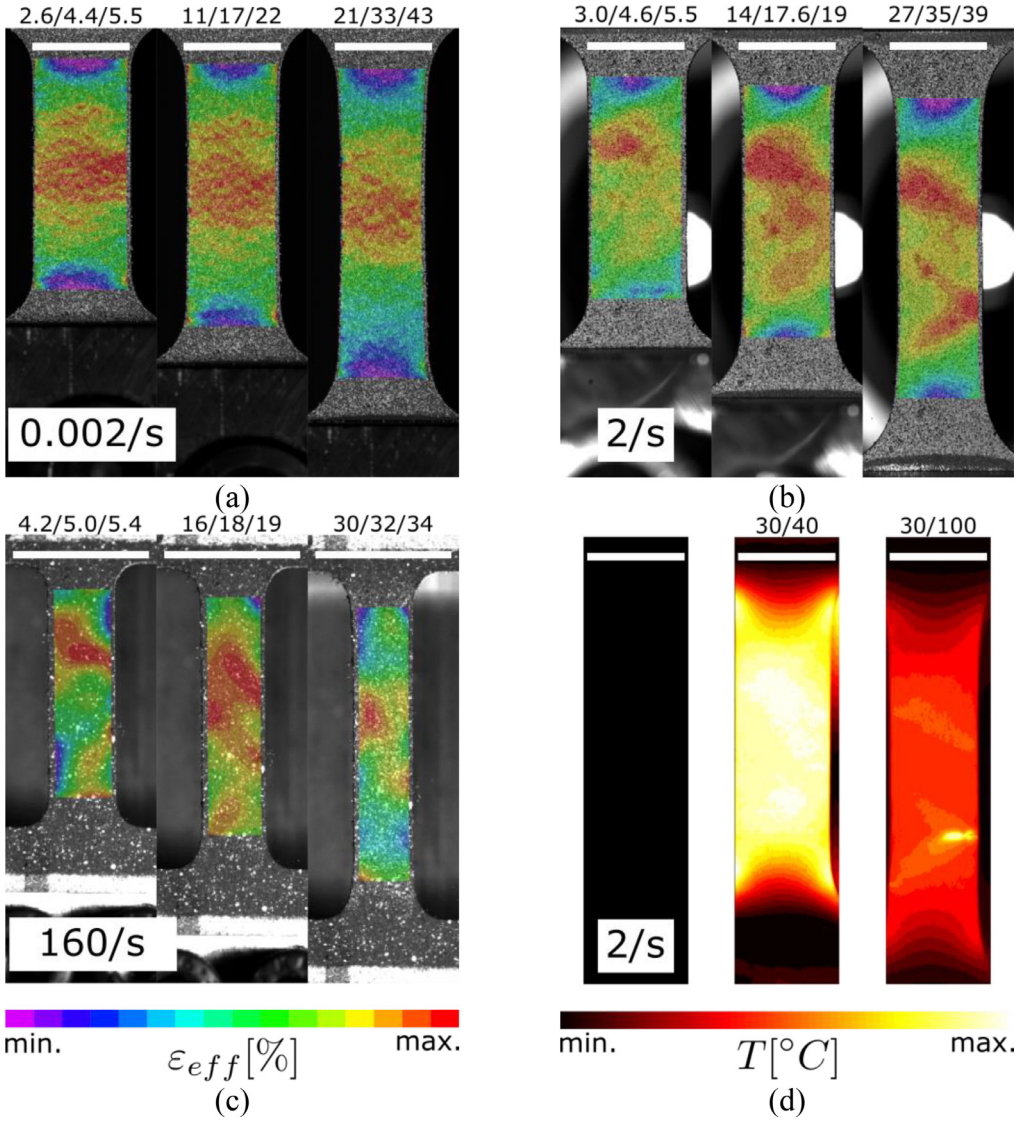

Fig. 9. Experimental logarithmic uniaxial strain fields at increasing macroscopic strain level: $\epsilon = 0.05$, $\epsilon = 0.20$ and at failure for (a) slow, (b) and (d) intermediate and (c) fast loading rate. The minimum, mean and maximum values of the strain are reported above each pictures. The strain field is heterogeneous even in the absence of engineering stress softening. (d) Shows the temperature field for the intermediate loading rate. The temperature increase is correlated with the high strain regions. The scale bar indicates a length of 10mm.

the deformation field. Furthermore, the fracture location is visible with a significant temperature rise close to the onset of failure. For the fast case, fracture initiates where deformation localized from the beginning of the test. Overall, the heterogeneity in the strain level prior to maximum force highlights the material heterogeneities with higher strain level in the region with higher void volume fraction. Final fracture occurs on the edge of the gauge section for most of the samples.

The fracture surface of one representative sample with high ductility (from batch #3) is compared with one representative of a low ductility specimen (lowest from batch #1) on Fig. 10. On both surfaces, and similar to the micro-CT, the voids are primarily arranged in layers corresponding to the binder deposition layers. Comparing the two specimens reveals the presence of very large voids in the less ductile specimen (Fig. 10a–c). Those pores are up to 200μm in width and around 50μm in height (along the build direction). The close-up view around one of the pores shows traces of intense plastic deformation with a high number of dimples. Furthermore, some particles can be found at the bottom of the dimples. It is speculated that these large voids are the origin of the early failure of the specimens. On the more ductile sample, the close-up view shows a high number of preexisting voids with smaller plastic dimples corresponding to void nucleation sites. No second-phase particles are visible at the center of the dimples. Thus, it is speculated that the failure is caused by the growth and coalescence of the pre-existing layered voids, which would explain the absence of softening in the UT experiments after maximum force.

4.2.2. *Results from experiments with complex stress states*

The measured normalized force-displacement and local axial strain response of the NT6 and SH specimens of the first three batches are presented in Fig. 11. The curves are truncated at the instant of visible surface crack on the images, which correlates to a sudden drop in force for the NT6. For reasons of comparability, accounting for the difference in thickness of the batches, the force is normalized by the measured thickness of each specimen. A small scatter is observed in the force-displacement and local strains at fracture within the same batch for the NT6 specimen. Similar to the results for uniaxial tension, batches #1 and #2 are comparable while batch #3 shows a lower force at the onset of plastic yield, a higher hardening rate and a larger displacement at

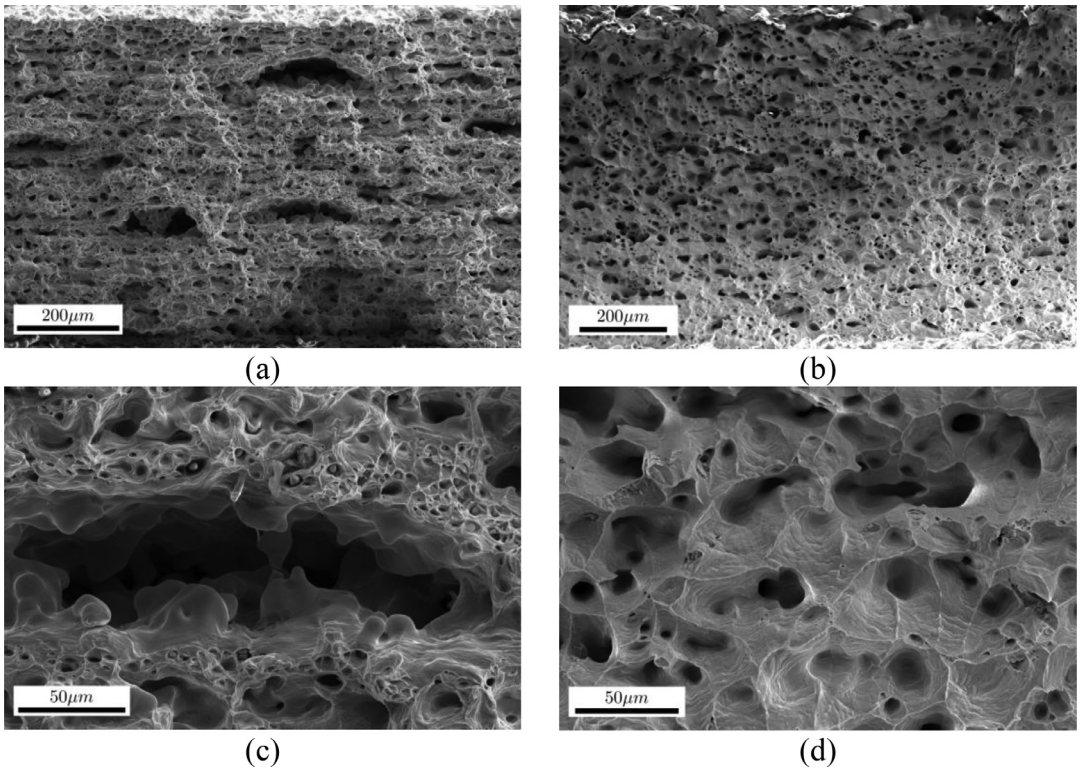

Fig. 10. Fracture surfaces of two UT0 samples highlighting the layered distribution of initial porosities at the specimen level and detailed views on the porosities showing a void coalescence behavior and smaller plastic dimples. (a) and (c) are representative of a sample with low ductility while (b) and (d) comes from a sample with high ductility.

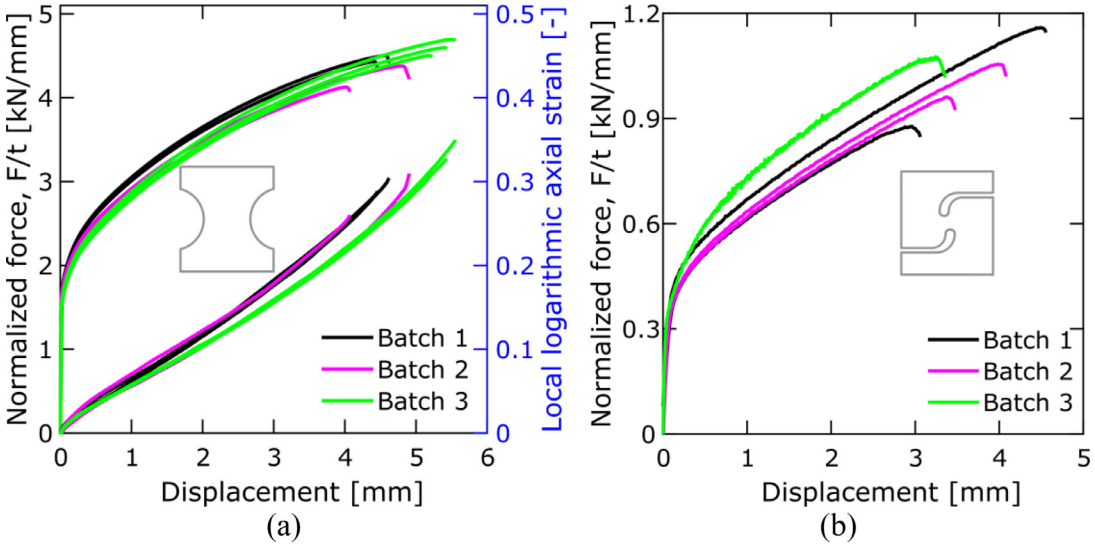

Fig. 11. Normalized force-displacement curves for the slow NT6 (a) and SH (b) for all three batches. A local log. strain measurement for a 2mm extensometer is shown for the NT6.

failure. The SH results exhibit more scatter in the measured force and displacement at failure for all batches which is tentatively attributed to the more pronounced effect of material heterogeneities in a small gauge section (as compared to the NT6). Fracture in the SH experiments initiates at maximum force and is localized outside the gauge section, possibly on the free edge subjected to uniaxial tension.

Due to the limited amount of material, the following experiments could only be carried out on batch #1. Fig. 12 shows the NT6 and SH response for different loading speeds along with the temperature evolution at selected locations on their surface. For the intermediate NT6, the temperature at the center of the gauge section (orange line) and on its edge (red line) is reported. For the fast NT6, only the temperature at the surface center is measured (blue dots). For the SH, the maximum temperature in the gauge section is shown. The general trend is similar to the one observed for the UT with higher forces and a decrease in displacement and local strain at failure, from 4.53mm to 4.40mm and 3.67mm for increasing speeds (NT6). The local strain evolution of the intermediate speed tests closely follows the one for the slow tests. The temperature evolves almost linearly for the NT6 at intermediate and high speeds before the last instants of the tests, where the temperature rises signif-

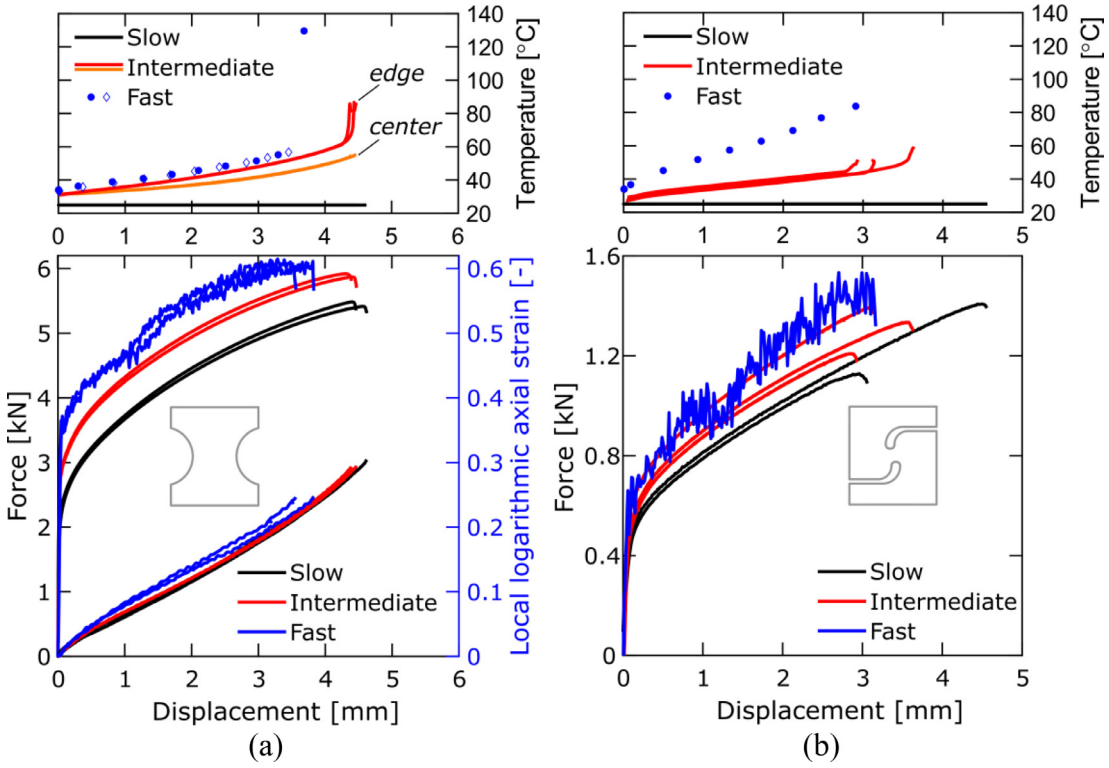

Fig. 12. Force-displacement curves at different strain rates for (a) the NT6 and (b) the SH. The top graphs show the temperature evolution at the center of the specimen surface.

icantly. For example, the intermediate NT6 edge temperature changes from 30°C to 60°C over the first 4.2mm of displacement and reaches 85°C at failure (4.37mm of displacement). The temperature evolution is similar for the intermediate and high speed NT6 experiments, differing only at the instant of significant rise and the last temperature measured. On the contrary, the evolution of the maximum temperature varies significantly for the intermediate and fast SH. While the displacements at fracture are similar, the maximum measured temperature changes from 55°C to 84°C.

The spatial distribution of the deformation at the last image before fracture initiation is presented in Fig. 13 for the NT6 and SH for all speeds. Due to the high hardening capability of the material and its low ductility, the deformation in the NT6 localizes on the outer edges of the gauge section rather than in the center (see for example [11]) and fracture initiates in this region. The high temperature region is located on the edge of the gauge section and shows the location of the future crack (similarly to the UT). Locally the effective strain at failure reaches values of 0.42, 0.42 and 0.39 near the notches with increasing loading speeds.

The strain field of the SH shows a strain concentration in the central part of the gauge section as well as on the tensile arms (bottom left and top right). Fracture initiates in these regions at a stress state close to uniaxial tension. The measured effective strain values of 0.55, 0.40 and 0.30 can only be considered as a lower bound of the effective strain at failure under shear. The maximum temperature reported is 44°C and it is distributed evenly between the different highly stretched regions. Fig. 14 shows the effective strain field at fracture initiation for the mini-punch (MP) and mini-Nakazima (MN) tests. For the MN, the deformation is localized below the knife-like punch with maximum values of 0.50 for both repeats. Final fracture initiates in the MN close to the chamfer on the free edges, similarly to the NT6 experiments. The strain field for the MP shows heterogeneous deformation at the center of the specimen with apex values about 0.48 and maximum values up to 0.8. These heterogeneities arise from the surface roughness of the specimen as well as the initial porosity distribution. The apex value is chosen as a lower bound of the fracture value under equi-biaxial tension as it corresponds to the only location with a well-defined stress state.

Table 1
Material parameters for elasto-plastic rate dependent material model.

$E[GPa]$	$\nu[-]$	$C_p[J/kgK]$	$\eta_k[-]$			
190000	0.3	449	0.9			
$P_{12}[-]$	$P_{22}[-]$	$P_{33}[-]$	$G_{12}[-]$	$G_{22}[-]$	$G_{33}[-]$	
-0.5	1.0	3.0	-0.456	1.034	2.926	
$A[MPa]$	$\epsilon_0[-]$	$n[-]$	$k_0[MPa]$	$Q[MPa]$	$\beta[-]$	$\alpha[-]$
1029.04	0.037	0.558	171.48	706.33	2.675	1.0
$C[-]$	$\dot{\epsilon}_0[1/s]$	$\dot{\epsilon}_a[1/s]$	$m[-]$	$T_0[^\circ C]$	$T_m[^\circ C]$	
0.0283	0.002	0.725	0.647	25	637	

4.3. Results from simulations

The direction-dependent Lankford ratios are presented in Fig. 7c. Using Eq. (21), the parameters of the flow potential are obtained. The hardening law is calibrated based on the response of a representative UT and is shown in Fig. 8 (black line). The calibration of the weighting parameter leads to the last plasticity parameter $\alpha = 1.0$, corresponding to a pure Swift law. All constitutive parameters including the strain-rate and temperature dependent ones solely based on batch #1 are summarized in Table 1.

The results of numerical simulations for the fracture experiments are presented in Fig. 15. The agreement with the experimental force displacement for the NT6 test at low strain rate is very good, with a maximum error in force of 0.04kN in the plastic range. The agreement at higher strain rate is also well captured with a maximum error of 0.07kN and 0.17kN for the intermediate and fast experiments. The predictive capability of the material model can be assessed on the local extensometer and temperature prediction of the NT6 as well as the SH. The simulated force-displacement response of the SH correlates with the experimental

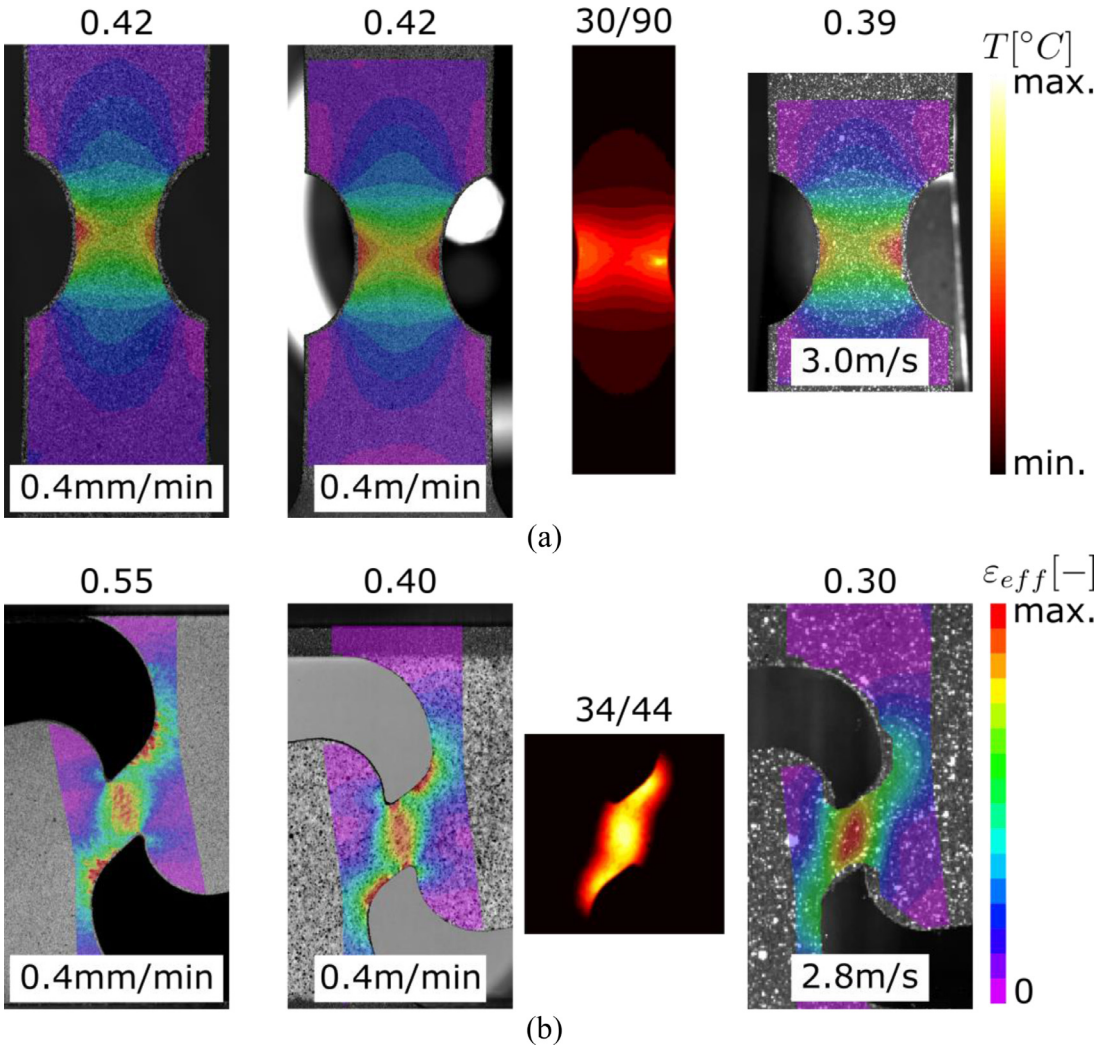

Fig. 13. Effective strain field from (a) NT6 and (b) SH experiment at fracture initiation. From left to right the loading speed increases. The intermediate loading speed feature a full field surface temperature image.

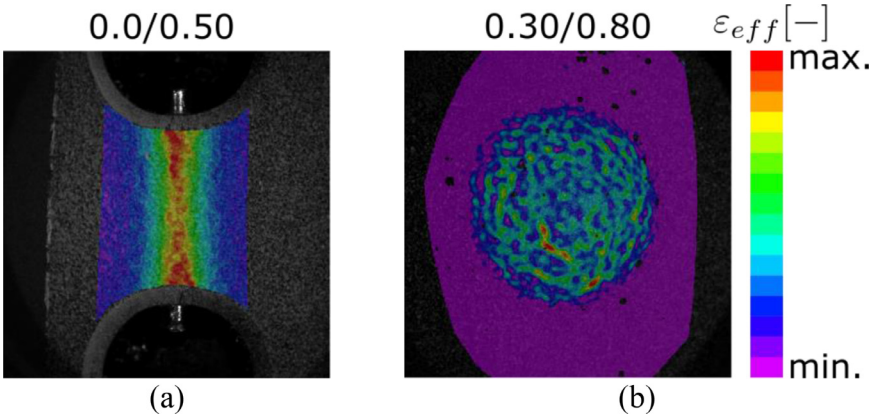

Fig. 14. Effective strain field from (a) MN and (b) MP experiment at fracture initiation.

results with the correct slope for slow and fast speeds with a slight offset of 0.025kN for the slow loading rate. However, the intermediate speed test exhibits a slight softening towards the end of the test which is not captured by the simulations. Here the maximum error reaches 0.06kN at the end of the simulation. Overall, the maximum error is less than 5% between the simulations and the experiments with regard to the force level.

Regarding the strain history, the material model captures the general trend of the higher local strain for higher strain rates and accurately captures the local strain for the slow experiments. For the fast tests, in the adiabatic range, the temperature evolution is accurately captured by the model with less than five degrees difference for both NT6 and SH and the correct slope. The same holds true for the local strains measured on the NT6 for which the offset starting at small displacements is tentatively

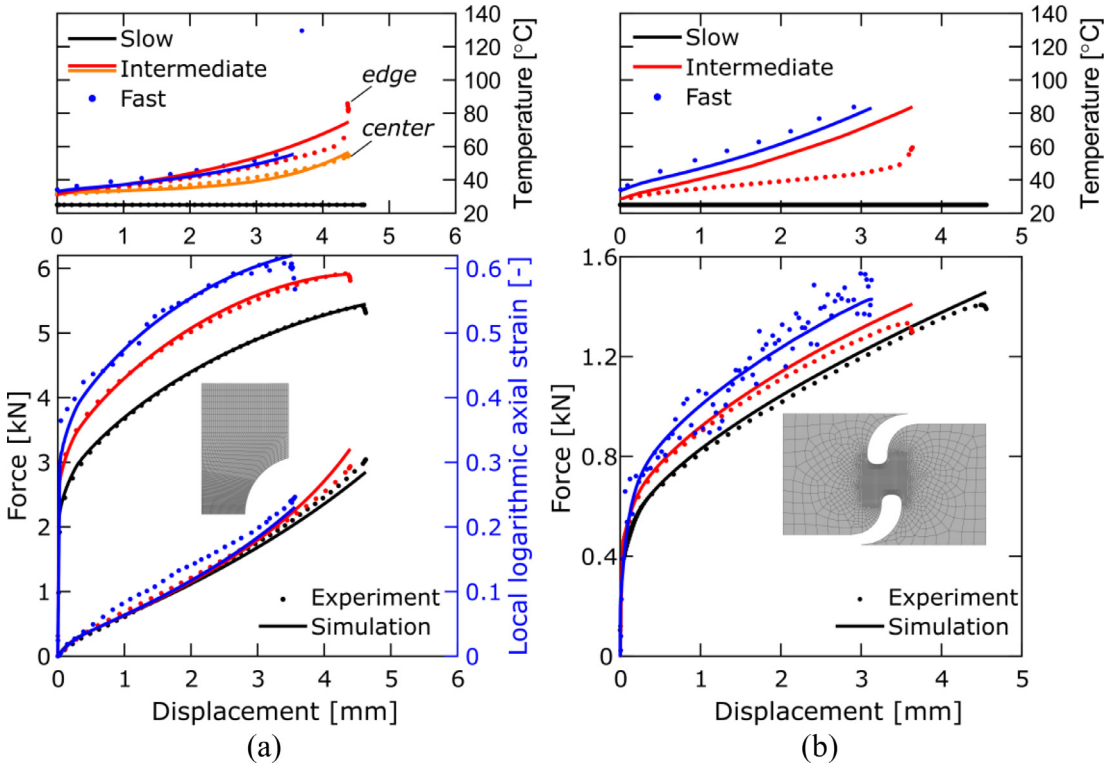

Fig. 15. Finite Element Analysis results. Comparison of the force, local strain and temperature evolution at different strain rates for the (a) NT6 and (b) SH.

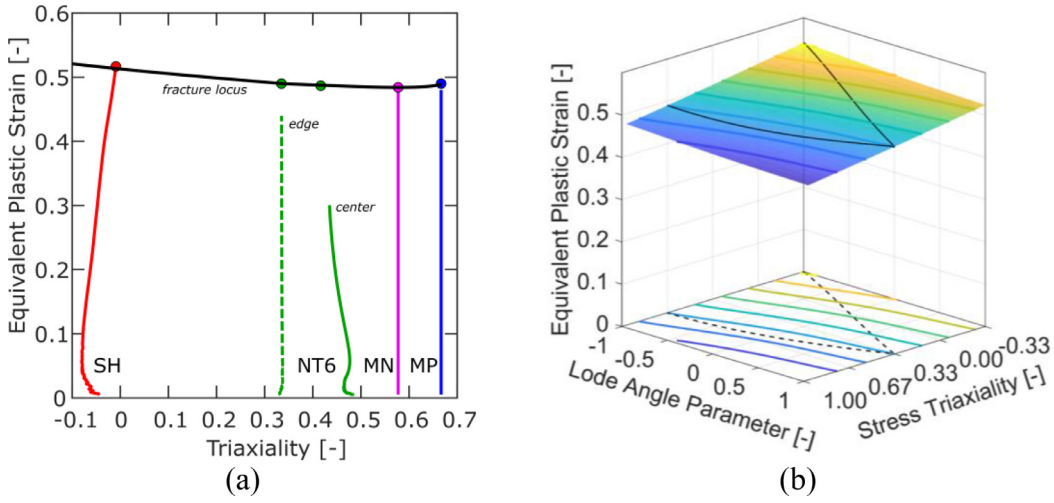

Fig. 16. Loading path to fracture for the NT6, SH, MN and MP specimen with calibrated fracture locus for proportional loading (a) for plane stress and (b) three dimensional locus.

attributed to inevitable inaccuracies in the set-up of the SHPB experiment with the load inversion device. The most significant differences are observed in the temperature evolution at intermediate speeds. For the NT6, the temperature in the center of the gauge section is predicted with good accuracy, however, the maximum temperature increase on the edge is overestimated, the difference in temperature reaching 10°C towards the end of the test. Similarly, the temperature evolution for the SH is too high compared with the experiments and resembles the one for the fast test.

The loading histories of the slow NT6 and SH are presented in Fig. 16a. The SH shows a proportional loading history with a triaxiality close to 0 (– 0.01 at fracture). Note that fracture initiates from the edge in the present study and thus the measured values should be seen as a lower bound of the failure under shear. For the NT6, loading paths are extracted from the central element along the midsection (full line) and on the outer edge along the midsection (dashed line) where fracture initiates. The latter material point follows a proportional loading history under uniaxial tension. The center of the midsection exhibits a lower equivalent plastic strain at fracture at a higher value of triaxiality (0.43 at fracture).

Using the loading history from these tests as well as the experimentally measured effective strain at fracture for the MN and MP, the Hosford-Coulomb parameters $a = 1.99$, $b = 0.49$ and $c = 0.005$ are obtained (see black line on Fig. 16 for the proportional loading history locus). The three-dimensional fracture locus (Fig. 16b) shows only minimal stress state dependence. The loading path on the edge of the NT6 exhibits a slightly earlier failure than the calibrated fracture initiation

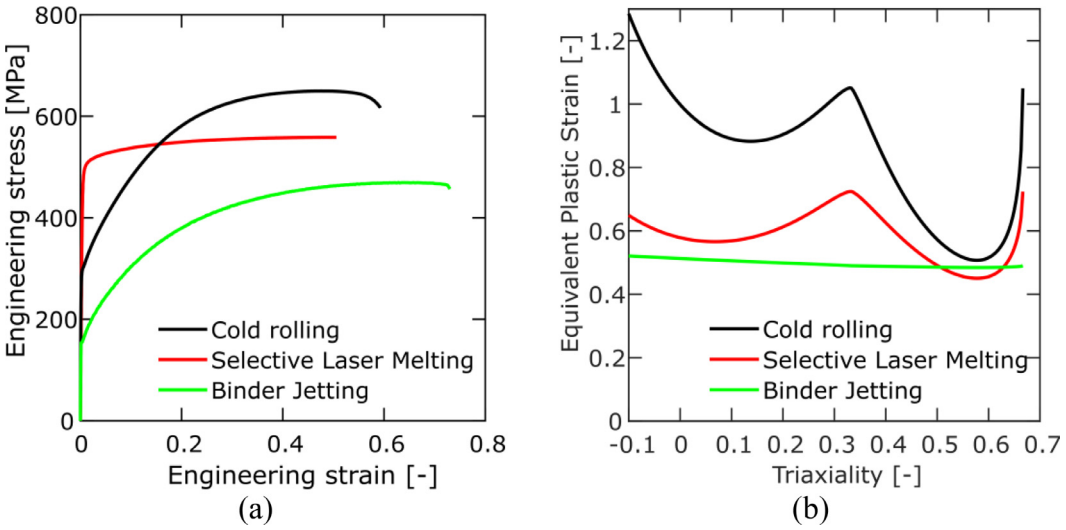

Fig. 17. Comparison of cold-rolled, SLM and binder jetting stainless steel 316L. (a) Engineering stress strain curve and (b) Hosford-Coulomb fracture locus. The corresponding results for the cold-rolled and SLM made 316L are taken from [30] and [11].

locus, while at this time the center of the NT6 has only reached a fraction of the fracture strain.

5. Conclusions

The mechanical properties of stainless steel 316L that is obtained through an additive binder-jetting process are experimentally characterized over a range of strain rates and stress states. The EBSD analysis shows that the material features large equi-axed grains with annealing twins. Micro-tomography images reveal a layered distribution of voids, which is associated with the layer-wise binder deposition. The initial void volume fraction reaches 3%. Due to the annealing during sintering, the material exhibits a low initial yield stress of around 160MPa, a strong hardening behavior with a hardening exponent close to 0.6 and a ductility ranging from 0.35 and 0.54 (engineering strains) for batches #1&2. The third batch exhibits a slightly lower yield stress (-8%) at higher hardening rate and ductility (0.46-0.75).

The comparison of the material obtained through binder-jetting with its cold-rolled counterpart [30] reveals a similar hardening behavior, but significantly lower strength (160 vs. 300MPa, Fig. 17a). When the same 316L alloy is made through selective laser melting (SLM, [11]) it exhibits a higher yield stress (about 500MPa), but a lower hardening rate than the binder-jetted and wrought materials. It is noteworthy that all three materials were tested in the same laboratory with similar methodologies. Multiple batches exhibited similar mechanical properties. The analysis of thick plates obtained through binder-jetting (10mm instead of 2*mm* for the standard batches) showed no significant through-thickness gradient in the mechanical properties.

The investigation of the large deformation behavior for strain rates covering five orders of magnitude (from 10^{-3}/s to 10^{2}/s) shows that the material features a moderate strain rate sensitivity (about +13MPa per strain rate decade for the yield stress). An anisotropic, rate-dependent plasticity model is identified based on the results of the notched tension experiments and validated on the shear experiments. The proposed plasticity model accurately captures the force displacement response of the material for all experiments and strain rates as well as the local strains. It further allows the fracture locus of the binder-jetted 316L to be identified through hybrid experimental-numerical analysis. As for the yield and hardening behavior, the material exhibits a much lower fracture locus compared to the cold-rolled and SLM counterparts (Fig. 17b), with a less pronounced Lode parameter dependence. This observation is attributed to the higher initial porosity of binder-jetted material which leads to faster void grow and coalesce at small strains.

Declaration of Competing Interest

The authors declare that they have no known competing financial interests or personal relationships that could have appeared to influence the work reported in this paper.

CRediT authorship contribution statement

Thomas Tancogne-Dejean: Data curation, Formal analysis, Investigation, Methodology, Visualization, Writing – original draft, Writing – review & editing. **Christian C. Roth:** Data curation, Formal analysis, Investigation, Methodology, Visualization, Writing – original draft, Writing – review & editing. **Dirk Mohr:** Supervision, Funding acquisition, Writing – review & editing.

Acknowledgement

The authors thank Mr. Nik Zielonka (ETH) for his help in performing the experiments and Mr. Knut Krieger (inspire AG) for his help with the metallographic specimen preparation. Partial funding from the MIT Industrial Fracture Consortium is acknowledged.

References

[1] Zegard T, Paulino GH. Bridging topology optimization and additive manufacturing. Struct Multidiscip Optim 2016;53:175–92. doi:10.1007/s00158-015-1274-4.
[2] Foust MJ, Thomsen D, Stickles R, Cooper C, Dodds W. Development of the GE aviation low emissions TAPS combustor for next generation aircraft engines. In: 50th AIAA Aerosp Sci Meet Incl New Horizons Forum Aerosp Expo; 2012. p. 1–9. doi:10.2514/6.2012-936.
[3] Herderick ED. Accelerating the Additive revolution. JOM 2017;69:437–8. doi:10.1007/s11837-017-2262-5.
[4] Khaing MW, Fuh JYH, Lu L. Direct metal laser sintering for rapid tooling: processing and characterisation of EOS parts. J Mater Process Technol 2001;113:269–72. doi:10.1016/S0924-0136(01)00584-2.
[5] Murr LE, Martinez E, Amato KN, Gaytan SM, Hernandez J, Ramirez DA, et al. Fabrication of metal and alloy components by additive manufacturing: examples of 3D materials science. J Mater Res Technol 2012;1:42–54. doi:10.1016/S2238-7854(12)70009-1.
[6] Agarwala M, Bourell D, Beaman J, Marcus H, Barlow J. Direct selective laser sintering of metals. Rapid Prototyp J 1995;1:26–36. doi:10.1108/13552549510078113.
[7] Bremen S, Meiners W, Diatlov A. Selective laser melting: a manufacturing technology for the future? Laser Tech J 2012;9:33–8. doi:10.1002/latj.201290018.
[8] Do T, Kwon P, Shin CS. Process development toward full-density stainless steel parts with binder jetting printing. Int J Mach Tools Manuf 2017;121:50–60. doi:10.1016/j.ijmachtools.2017.04.006.
[9] Mirzababaei S, Pasebani S. A review on binder jet additive manufacturing of 316L stainless steel. J Manuf Mater Process 2019;3:8–12. doi:10.3390/jmmp3030082.

[10] Zwiren A, Murphy TF. Comparison of Binder Jetting Additive Manufacturing to Press and Sinter 316L Stainless Steel. Int. J. Powder Metall. 2018;54.
[11] Li X, Roth CC, Tancogne-Dejean T, Mohr D. Rate- and temperature-dependent plasticity of additively manufactured stainless steel 316L: characterization, modeling and application to crushing of shell-lattices. Int J Impact Eng 2020;145:103671. doi:10.1016/j.ijimpeng.2020.103671.
[12] Riemer A, Leuders S, Thöne M, Richard HA, Tröster T, Niendorf T. On the fatigue crack growth behavior in 316L stainless steel manufactured by selective laser melting. Eng Fract Mech 2014;120:15–25. doi:10.1016/j.engfracmech.2014.03.008.
[13] Bronkhorst CA, Mayeur JR, Livescu V, Pokharel R, Brown DW, Gray GT. Structural representation of additively manufactured 316L austenitic stainless steel. Int J Plast 2019;118:70–86. doi:10.1016/j.ijplas.2019.01.012.
[14] Wilson-Heid AE, Qin S, Beese AM. Multiaxial plasticity and fracture behavior of stainless steel 316L by laser powder bed fusion: experiments and computational modeling. Acta Mater 2020. doi:10.1016/j.actamat.2020.08.066.
[15] Li Z, Voisin T, McKeown JT, Ye J, Braun T, Kamath C, et al. Tensile properties, strain rate sensitivity, and activation volume of additively manufactured 316L stainless steels. Int J Plast 2019;120:395–410. doi:10.1016/j.ijplas.2019.05.009.
[16] Kumar P, Jayaraj R, Suryawanshi J, Satwik UR, McKinnell J, Ramamurty U. Fatigue strength of additively manufactured 316L austenitic stainless steel. Acta Mater 2020;199:225–39. doi:10.1016/j.actamat.2020.08.033.
[17] Soleimani M, Kalhor A, Mirzadeh H. Transformation-induced plasticity (TRIP) in advanced steels: a review. Mater Sci Eng A 2020;795:140023. doi:10.1016/j.msea.2020.140023.
[18] Paredes M, Grolleau V, Wierzbicki T. On ductile fracture of 316L stainless steels at room and cryogenic temperature level: an engineering approach to determine material parameters. Materialia 2020;10:100624. doi:10.1016/j.mtla.2020.100624.
[19] Roth CC, Mohr D. Determining the strain to fracture for simple shear for a wide range of sheet metals. Int J Mech Sci 2018;149:224–40. doi:10.1016/j.ijmecsci.2018.10.007.
[20] Roth CC, Mohr D. Ductile fracture experiments with locally proportional loading histories. Int J Plast 2016. doi:10.1016/j.ijplas.2015.08.004.
[21] Grolleau V, Roth CC, Lafilé V, Galpin B, Mohr D. Loading of mini-Nakazima specimens with a dihedral punch: determining the strain to fracture for plane strain tension through stretch-bending. Int J Mech Sci 2019;152:329–45. doi:10.1016/j.ijmecsci.2019.01.005.
[22] Roth CC, Gary G, Mohr D. Compact SHPB system for intermediate and high strain rate plasticity and fracture testing of sheet metal. Exp Mech 2015;55:1803–11. doi:10.1007/s11340-015-0061-x.
[23] Swift HW. Plastic instability under plane stress. J Mech Phys Solids 1952;1:1–18. doi:10.1016/0022-5096(52)90002-1.
[24] Voce, E. The relationship between stress and strain for homogeneous deformations, 1948.
[25] Sung JH, Kim JH, Wagoner RH. A plastic constitutive equation incorporating strain, strain-rate, and temperature. Int J Plast 2010;26:1746–71. doi:10.1016/j.ijplas.2010.02.005.
[26] Pack K, Roth CC. The second Sandia fracture challenge: blind prediction of dynamic shear localization and full fracture characterization. Int J Fract 2016. doi:10.1007/s10704-016-0091-0.
[27] Johnson GR, Cook WH. A Constitutive Model and Data for Metals Subjected to Large Strains, High Strain Rates, and High Temperatures. 7th International Symposium on Ballistics, The Hague, 19-21 April 1983 1983:541–7.
[28] Roth CC, Mohr D. Effect of strain rate on ductile fracture initiation in advanced high strength steel sheets: EXPERIMENTS and modeling. Int J Plast 2014. doi:10.1016/j.ijplas.2014.01.003.
[29] Mohr D, Marcadet SJ. Micromechanically-motivated phenomenological Hosford–Coulomb model for predicting ductile fracture initiation at low stress triaxialities. Int J Solids Struct 2015;67–68:40–55. doi:10.1016/j.ijsolstr.2015.02.024.
[30] Bonatti C, Mohr D. Mechanical performance of additively-manufactured anisotropic and isotropic smooth shell-lattice materials: simulations & experiments. J Mech Phys Solids 2019;122:1–26. doi:10.1016/j.jmps.2018.08.022.